JOURNAL OF SYNCHROTRON RADIATION

ISSN 1600-5775

A versatile X-ray phase retarder for lock-in XMCD measurements

Eduardo H. T. Poldi,[a,b] Carlos A. Escanhoela Jr,[a] Jairo Fonseca Jr,[a] Marcos A. S. Eleotério,[a] Ricardo D. dos Reis,[a] Jonathan C. Lang,[c] Daniel Haskel[c] and Narcizo M. Souza-Neto[a]*

[a]Brazilian Synchrotron Light Laboratory, Brazilian Center for Research in Energy and Materials, Campinas, Sao Paulo 13083-970, Brazil, [b]Institute of Physics 'Gleb Wataghin', University of Campinas, Campinas, Sao Paulo 13083-860, Brazil, and [c]Advanced Photon Source, Argonne National Laboratory, Argonne, IL 60439, USA. *Correspondence e-mail: narcizo.souza@lnls.br

Received 19 February 2020
Accepted 13 July 2020

Edited by A. F. Craievich, University of São Paulo, Brazil

Keywords: XMCD; phase retarder; lock-in; dichroism; XAS; instrumentation; X-ray spectroscopy; magnetism.

X-ray magnetic circular dichroism (XMCD) is a technique commonly used to probe magnetic properties of materials with element and orbital selectivity, which requires the use of circularly polarized (CP) X-rays. It is possible to accomplish XMCD experiments with fixed CP and alternating the magnetic field orientation, but most reliable data are obtained when alternating the magnetization orientation and the polarization between right and left helicities. A versatile strategy has been developed to perform XMCD experiments using a hard X-ray quarter-wave plate, at both polychromatic dispersive and conventional monochromatic optics, in combination with synchronous data acquisition. The switching frequency waveform is fed into a lock-in amplifier to detect and amplify the XMCD signal. The results on a reference sample demonstrate an improvement in data quality and acquisition time. The instrumentation successfully generated 98% of CP X-rays switching the beam helicity at 13 Hz, with the possibility of faster helicity switching once it is installed at the new Brazilian fourth-generation source, SIRIUS.

1. Introduction

X-ray magnetic circular dichroism (XMCD) is an element-selective technique used to study magnetic compounds (Schütz *et al.*, 1987; Chen *et al.*, 1995; Stöhr, 1999), with the dichroic signal occurring near the Fermi level due to a difference in spin-up and spin-down unoccupied states probed in the X-ray absorption process. An XMCD signal is generally obtained as the difference between two absorption spectra (XAS) of circularly polarized X-rays with opposite helicities, with an applied magnetic field along the X-ray beam propagation axis to either induce an alignment of sample magnetic moments in the case of ferro/ferrimagnetic and paramagnetic systems, or induce an imbalance between spin up and down density of states near the Fermi level in the diamagnetic systems.

In the hard X-ray range, XMCD signals have amplitudes of only a small fraction of the absorption jump, with signals spanning the 10^{-1} to 10^{-4} range (Odin *et al.*, 1998; Mathon *et al.*, 2004; Lamirand *et al.*, 2013). To perform XMCD measurements one can either switch the beam helicity (between left and right circularly polarized) or the magnetic field orientation (parallel or anti-parallel to the beam direction). A fast switching of the polarization or field can be used to achieve good signal-to-noise ratio. However, while fast field switching can impose difficulties particularly for hard magnetic materials where large magnetic fields are required,

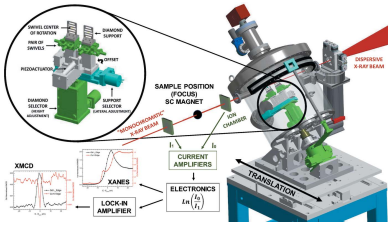

fast polarization switching has been efficiently implemented in the past with phase plates (Hirano *et al.*, 1992), which also allows field-dependent (hysteresis) XMCD measurements.

One can obtain circularly polarized X-rays directly from the synchrotron radiation source, for example with an elliptically polarizing undulator or using out-of-orbit elliptical polarization from dipole radiation (Tolentino *et al.*, 2005). Another way of producing circularly polarized X-rays is by a quarter-wave plate (QWP). A perfectly single-crystalline QWP (Belyakov & Dmitrienko, 1989), in our case diamond single crystals, exhibits X-ray birefringence in the vicinity of the Bragg peak giving rise to phase shifts between the σ- and π-beam polarization components propagating through the crystal (Hirano *et al.*, 1991, 1993; Lang & Srajer, 1995). In order to attain better beam stability, microfocusing and fast collection of XMCD spectra, previous implementations combined diamond QWP with dispersive optics (Giles *et al.*, 1994), due to its static (non-scanning) dispersive monochromator and area detector (CCD) (Cezar *et al.*, 2010).

The beam footprint at the location of the QWP depends on the size of the magnet used to perform the experiment which defines the distance between the focal point of the polychromator (magnet center) and the QWP. While a large-enough single-crystalline diamond QWP (compatible with conventional dispersive geometry) may come at a high cost, it may also be very difficult to find in nature or produce artificially. In our case, the horizontal beam footprint at 1 m before the sample is about 90 mm at 7 keV, as shown later in Fig. 2. Additionally, the conventional dispersive optics acquisition based on area detectors (Tolentino *et al.*, 2005) is not compatible with the fast helicity switching (Hirano *et al.*, 1992) linked with a lock-in amplification (Suzuki *et al.*, 1999) due to the inability to acquire the incident and transmitted beams concomitantly. To overcome these limitations, here we combine an energy scanning strategy with dispersive optics (Pascarelli *et al.*, 1999), together with a regular-size diamond QWP switching at tens of Hertz and lock-in data acquisition, for high stability and high signal-to-noise ratio XMCD measurements. This combination enables use of large magnets at the beamline, with no need for big and expensive single-crystalline diamond phase plates.

2. Experimental setup

This instrumentation was developed to be used at the dispersive geometry dipole-based D06A-DXAS beamline (Dispersive X-ray Absorption Spectroscopy) (Cezar *et al.*, 2010) as well as at the monochromatic non-dispersive wiggler-based W09A-XDS beamline (X-ray Diffraction and Spectroscopy) (Lima *et al.*, 2016) of the 1.34 GeV UVX second-generation source of the Brazilian Synchrotron Light Source (LNLS). In addition, it was planned to be compatible without modifications with the monochromatic-based EMA beamline (extreme condition) of SIRIUS, the 3 GeV fourth-generation synchrotron source of LNLS under commissioning. To be compatible with all three beamlines, we based the setup and vacuum chamber on the previous report of Suzuki *et al.* (2014), with modifications to allow the energy scanning, fast helicity switching, lock-in noise-filtering and capable of holding several QWPs. This setup is represented in Fig. 1.

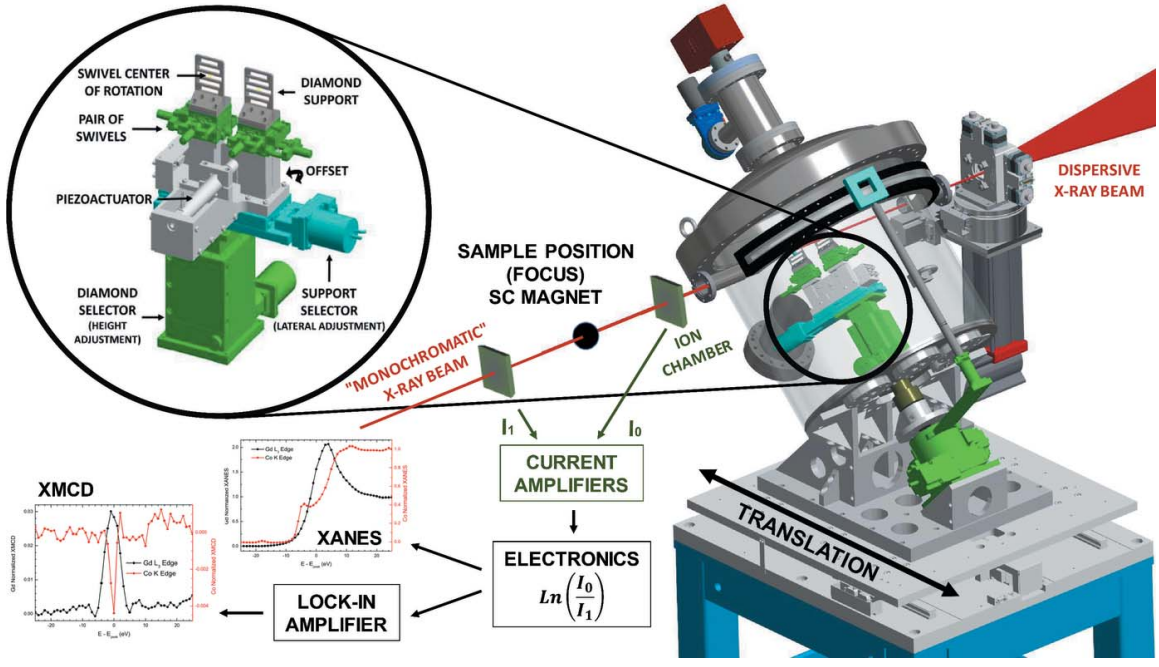

Figure 1
QWP experimental setup representation, with a vacuum chamber. This chamber is required at the EMA beamline at SIRIUS because the setup is directly connected to the beamline vacuum. The inset details the motors assembly, which can be used for alignment corrections during an XMCD experiment, and the support for up to ten diamond QWPs with different thicknesses to access different energy ranges. This schematic describes how a slit scans the dispersive beam for energy selection to allow integrating transmission detectors (photodiodes, in this case) to be used for lock-in detection, not possible with conventional dispersive optics.

In a monochromatic geometry, a lock-in noise-filtering can be achieved using a piezo actuator (PZT) to quickly offset the QWP's angular position from the Bragg angle, therefore flipping the beam polarization between circular left and circular right. To oscillate between the QWP angular positions for maximum degree of circular polarization (P_C), we connected the PZT to a square-wave generator and used this waveform as the reference signal for a lock-in amplifier. The latter acts as a Fourier transform frequency filter, removing all noise with frequencies other than the reference. The input signal to the lock-in amplifier is the logarithm of the ratio between the initial (I_0) and transmitted (I_1) beam intensities computed with a log-divider module designed at Argonne (B. Deriy *et al.*, unpublished; Suzuki *et al.*, 1998). The lock-in outputs a signal with amplitude proportional to the difference in X-ray absorption for opposite helicities; *i.e.* the XMCD signal. Here we implemented this noise-filtering XMCD measurement not only for the monochromatic beamlines (XDS and EMA), as commonly used, but also made it compatible with the dispersive geometry of the DXAS beamline.

In order to combine the dispersive geometry and the lock-in noise-filtering, we introduce a slit after the polychromator to scan the incident polychromatic horizontally dispersive beam, similarly to the turbo-XAS method described by Pascarelli *et al.* (1999). After this slit, we insert the QWP chamber to switch the beam helicity (Fig. 1). The slit defines and selects an energy bandwidth (δE) small enough for the beam to be considered monochromatic at each slit position, given the dispersive geometry contributions to the energy resolution $\delta E_{\rm opt}$ (Cezar *et al.*, 2010). Then, $\delta E = [(\delta E_{\rm opt})^2 + (\delta E_{\rm s})^2]^{1/2}$, where $\delta E_{\rm s}$ is the slit aperture contribution to the total energy resolution. One can estimate the latter term using the relation $\delta E_{\rm s}/\Delta E = \delta L_{\rm s}/\Delta L$, where ΔE is the total energy bandwidth passing through a large region with length ΔL, at the slit position, which has a small aperture $\delta L_{\rm s}$. Additionally, this monochromatic beam emerging from the slit must fit completely and be centered in the QWP along the entire translation range. Nevertheless, there is a limitation associated with the distance from the QWP to the slit, since this limitation occurs due to a misalignment (ΔX) between these two elements as the beam angle changes with the slit scan (as schematized in Fig. 2). Therefore, a relative slit translation (correction) is required to maintain the QWP centered at the beam through an entire energy scan. Fig. 2 also presents calculations for the bandwidth as a function of both QWP width and distance from the QWP to the slit, according to $B_{\rm QWP} = \{(B_{\rm b}q)/[F_{\rm b}(S-d)]\}\, w_{\rm QWP} \sin\theta_{\rm B}$, where $B_{\rm QWP}$ is the energy bandwidth accepted by the QWP, $B_{\rm b}$ is the beamline bandwidth (total energy range covered by the polychromator), q is the distance from the polychromator to the focus, $F_{\rm b}$ is the beam footprint, $(S-d)$ is the QWP-to-slit distance, $w_{\rm QWP}$ is the QWP horizontal size, and $\theta_{\rm B}$ is the QWP Bragg angle. Thus, we can better visualize in Fig. 2 the relationship between these elements. In our case, using a QWP size of 5 mm × 5 mm ($w_{\rm QWP}$ = 5 mm) a total energy bandwidth of ∼400 eV was obtained with a QWP-to-slit distance ($S-d$) ≃ 7 cm (red line). With an increase in ($S-d$), the total energy bandwidth

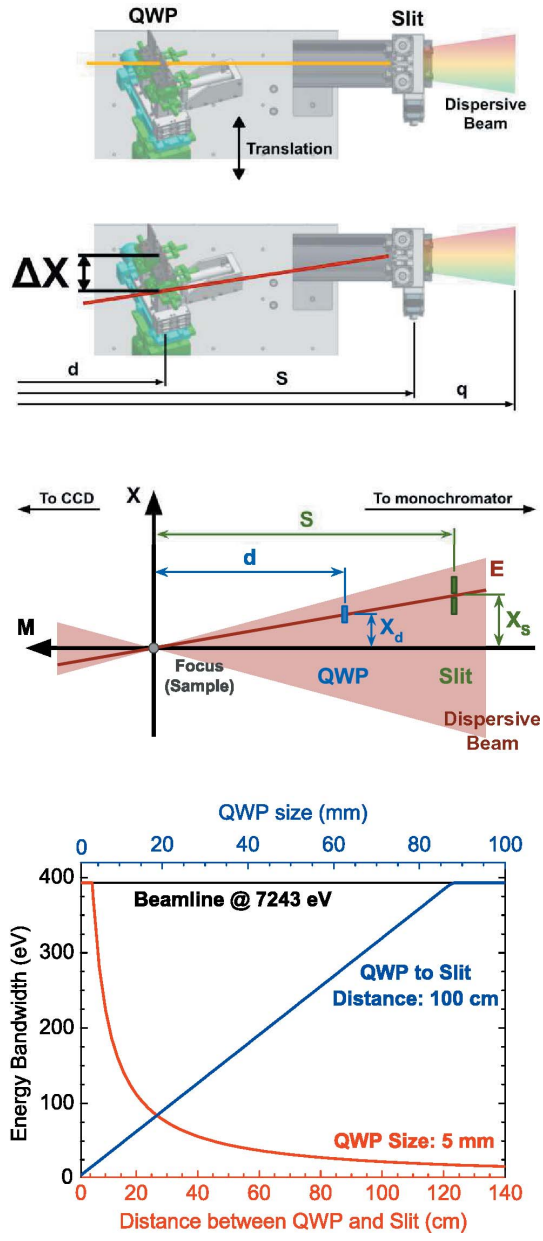

Figure 2
Top: instrumentation shown in Fig. 1 (top view, without the vacuum chamber) in situations that dispersive optics could make the beam pass or not through the QWP. In the case of this instrumentation, $S \gg d$. So as the slit scans across the dispersive beam, there is a condition when the beam does not hit the QWP. This alignment limitation causes the short spectral energy bandwidth, requiring a relative slit translation to maintain the QWP centered at the beam through an entire energy scan. Middle: representation of the elements used to elaborate the correction for the QWP positioning. An X-ray beam with energy E selected by the slit at a distance S from focus, positioned at an $X_{\rm S}$ with respect to the translation axis X. The QWP ideal position is then $X_{\rm d}$, at a distance d from the focal point. Then, equation (1) is obtained using the relation for energy resolution in space: $\Delta E/E = \Delta L/L$, and substituting $L = SX/M$ (because the energy bandwidth ΔL is selected at S), where X and M are variables in directions X and M. Bottom: DXAS beamline energy bandwidth (black line) at a fixed energy of 7243 eV, p = 9.75 m and q = 1.5 m; and theoretical calculation for the bandwidth available for the XMCD experiment (red line), as a function of the distance from the QWP (∼5 mm × 5 mm) to the slit. The blue line is the bandwidth calculation as a function of the QWP size, for the same energy of 7243 eV, at a fixed distance of 100 cm between the QWP and the slit.

drops. We can also calculate the required w_{QWP} needed to maintain the sample total energy bandwidth for a given $(S - d)$ (blue line). For example, at $(S - d) = 100$ cm, the QWP size is $w_{QWP} \simeq 90$ mm.

These monochromatic beam conditions allow conventional intensity monitors to be used (ionization chambers or photodiodes) to acquire the fast response of I_0 and I_1 simultaneously, which is fundamental for the lock-in noise-filtering. The QWP setup is placed between the slit and the first ionization chamber, as shown in Fig. 1. Considering both elements for a complete XMCD experimental setup, a large superconducting magnet (radius usually larger than 250 mm) and QWP vacuum chamber (in this case with radius of ~200 mm), and a distance from the polychromator to the focus of 1.5 m, this setup would have a very small spectral energy range (about 20 eV). Thus, to maximize this range it would be necessary to move the phase retarder closer to the slit or to move the QWP closer to the sample. However, due to the superconducting magnet size, the QWP chamber needs to be as close as possible to the slit; and, for better energy resolution, the distance between the slit and polychromator needs to be as small as possible. Then, to increase the experiment energy range an algorithm was implemented: it concomitantly translates both slit and QWP according to the beam trajectories using triangles similarity. Looking at Fig. 2, the energy can be defined by the position of the slit aperture relative to the translation table, thus guaranteed the beam to always pass through the phase plate center. This implies that the energy of an X-ray beam at the position X with distance to the focus M is given by

$$E(M, X) = \frac{\Delta E}{\Delta L}\frac{S}{M}X, \tag{1}$$

where ΔE and ΔL are taken at the slit position S. Therefore, the misalignment (ΔX) for a specific energy would be due to the difference between the beam position as if the QWP was placed exactly at the slit position (S) instead of its real position (d), or simply

$$\Delta X(E, S, d) = X_S - X_d = \frac{\Delta L}{\Delta E}E - \frac{\Delta L}{\Delta E}\frac{S}{d}E = \frac{\Delta L}{\Delta E}\frac{E}{S}(S - d), \tag{2}$$

and the corrected energy would be

$$E(\Delta X, S, d) = \frac{\Delta E}{\Delta L}\frac{S}{(S - d)}\Delta X. \tag{3}$$

This relative slit translation allowed us to enlarge the energy range of the XAS and XMCD spectra, from about 20 eV to the total beamline bandwidth as described above (~400 eV at 7 keV for this case). Here we note that although spectra with a range of 400 eV can be achieved, we chose to scan only with 50 eV for better contrast with that previously obtained with 20 eV. Fig. 3 compares XANES spectra before and after the correction was implemented. To perform an XMCD spectrum, we have to scan the energy by moving the slit and concomitantly track the Bragg angle and the QWP relative position for each point of energy according to equation (2). Consequently,

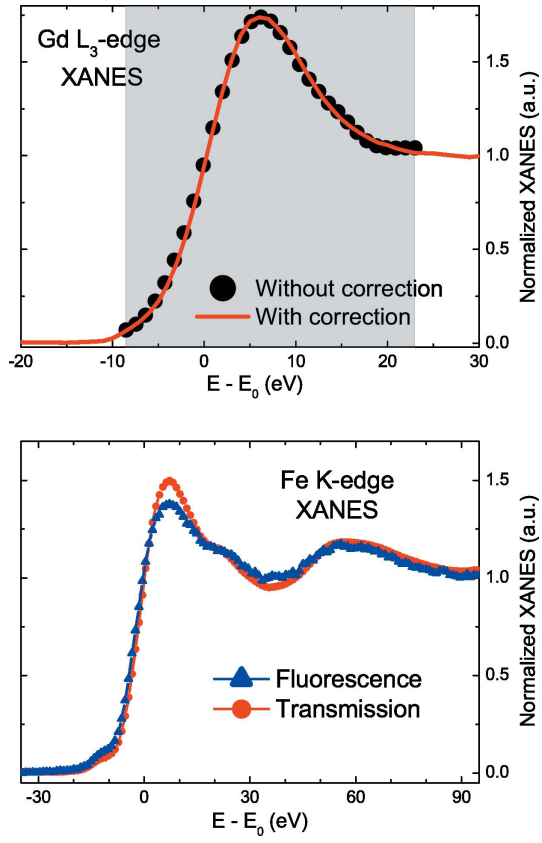

Figure 3
Top: comparison between the spectra obtained with and without implementing the energy/position correction as derived in the main text. Differences in the shape of the absorption edge and white line are due to different apertures of the slit and normalization conditions between these experiments. Bottom: fluorescence-mode XAS of the Fe K-edge on a Fe_2O_3 sample obtained at the dispersive beamline compared with its transmission-mode counterpart. The distortions in the fluorescence data are probably due to self-absorption.

the implementation and automation of the slit correction allows us to use small diamond plates, which are easier to find and cheaper, even in the case of very large distances between the QWP and the focal plane, and use a large superconducting magnet such as the one we have available to reach fields of up to 6 T. Moreover, as a result of this implementation, we are also able to obtain an XAS spectrum in fluorescence mode at our dispersive XAS beamline at LNLS. This is demonstrated in Fig. 3, where we show a comparison between transmission and fluorescence absorption spectroscopy at the Fe K-edge of a Fe_2O_3 sample. The differences in the white line between the two spectra are related to the self-absorption process, inherent of the fluorescence detection. We note that this new instrumentation opens up an opportunity for us to obtain the XMCD spectrum using fluorescence mode, for samples that require such type of detection.

3. Polarization characterization of a Bragg transmission phase plate at monochromatic condition

An X-ray QWP, or phase plate, is a crystal that presents sizable birefringence near absorption edges or near Bragg

reflections. In this work we used diamond single-crystalline QWPs. This means that the index of refraction depends on the relative orientation of the electric field (polarization) and diffracting Bragg planes. Near the Bragg condition, the σ- and π-polarized X-rays propagate with different phase velocities inside the crystal, inducing a phase retardation between them. Its properties cannot be described by the kinematical theory of X-ray diffraction, requiring the dynamical approach (Belyakov & Dmitrienko, 1989). For Bragg geometry, the phase difference (δ) between σ- and π-components, due to an offset of $\Delta\theta$ from the Bragg angle (θ_B), is

$$\delta = -\frac{\pi}{2}\left(\frac{r_e}{\pi V}\right)^2 \frac{\lambda^3 t\, \Re[F_h F_{\bar{h}}]}{\Delta\theta}\frac{\sin 2\theta_B}{\sin\theta}, \qquad (4)$$

where t is the plate thickness, λ is the incident photon wavelength, r_e is the classical electron radius, V is the unitary cell volume and F_{hkl} is the structure factor associated with the (h, k, l) Miller indices. Considering a perfectly monochromatic and parallel beam, for a phase retardation of $\pi/2$, we have $\Delta\theta = \mp(r_e/\pi V)^2\lambda^3 t\,\Re[F_h F_{\bar{h}}](\sin 2\theta_B/\sin\theta)$, and then

$$P_C = \frac{2(I_H I_V)^{1/2}}{I_H + I_V}, \qquad (5)$$

where I_H and I_V are the transmitted beam intensities with electric field polarization components in the horizontal and vertical directions, respectively. The initial goal was to measure I_H and I_V of X-rays generated after the propagation through the QWP. Then, using equation (5), we experimentally determined P_C and the angular offset for maximum P_C. These intensities were measured via Thomson scattering by air, as Fig. 4 shows, placing a detector above the X-ray beam path to monitor the intensity in the vertical plane, which corresponds to I_H; and a detector on the side of the X-ray beam to capture the intensity scattered in the horizontal plane, which corresponds to I_V. To perform these experiments, the beamline optics had to be configured to provide beam divergence of 30 µrad = 0.00172°, similar to the FWHM (full width at half-maximum) intrinsic width of the diamond Bragg reflection. The QWP commissioning was performed at the conventional double-crystal monochromator geometry wiggler-based W09A-XDS beamline (Lima *et al.*, 2016), similarly to previous applications of QWPs at non-dispersive beamlines (Hirano *et al.*, 1992; Boada *et al.*, 2010). We have chosen for the commissioning a 400 µm-thick diamond plate, oriented in the (111) direction, which has easily achievable values for its Bragg angle and offset for maximum P_C at 9 keV, for which the beamline flux is optimum (about 10^{11} photons s^{-1}). The transmitted intensity through the QWP as it is rocked through the Bragg peak is shown in Fig. 4 (black dots). The FWHM is 0.0131°, given by a Lorentzian fit of the experimental data. This width is larger than that expected due to a large photon source size (~100 µm) at the W09A port of the UVX second-generation source which affects the vertical beam divergence and, therefore, the beamline energy resolution beyond the intrinsic. Even under these conditions, this Bragg peak was sharp enough to successfully produce a

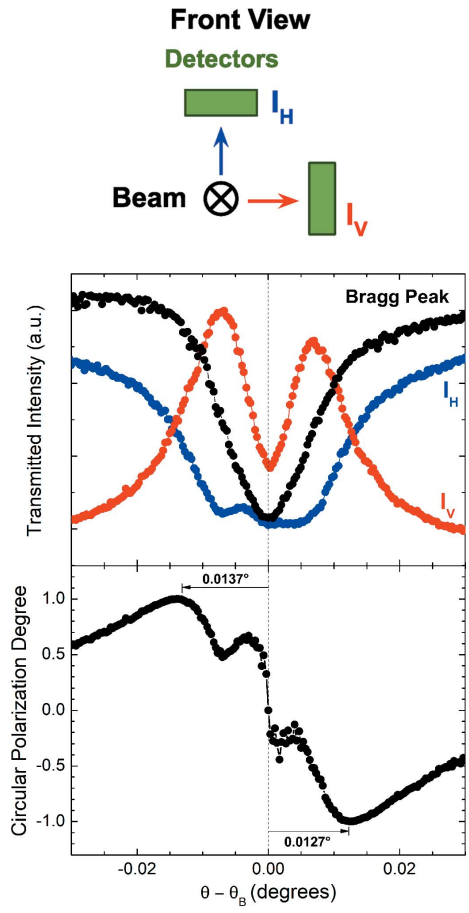

Figure 4
Top: schematic of I_V and I_H measurements via elastic scattering by air, using detectors (photodiodes) positioned above and beside the X-ray beam. Bottom: 400 µm-thick diamond plate Bragg peak and intensities associated with the polarization components for an incoming X-ray beam with 9 keV energy. The distance between peaks of vertical polarization (red curve) shows that the offset from the Bragg angle to reach maximum P_C is approximately 0.0134°; and experimental curve for circular polarization degree. The data show that ~98% of circular polarization was achieved using the 400 µm-thick C(111) plate.

circular polarized beam. Fig. 4 shows X-ray intensities I_V (red dots) and I_H (blue dots), as a function of the QWP angular offset, demonstrating the X-ray polarization state varying with changes in the offset from the Bragg angle. The vertical polarization component, I_V, has low intensity at angles far from the Bragg peak, gradually increasing until a maximum as the QWP angle nears the Bragg condition, symmetrically with respect to Bragg angle. It peaks at a certain angle and the distance between these angles is 0.0134°. For the maximum degree of vertical polarization we need a phase difference of 180°; while, for P_C, the phase difference must be 90°, so the offset for P_C is twice the offset for vertical polarization [phase is linear with $\Delta\theta$, see equation (4)]. Therefore, the angular distance between the red curve peaks corresponds to the angular offset for maximum P_C. Thus, we are able to determine the circular polarization, from equation (5) and shown in Fig. 4 (bottom), greater than 98% with an angle offset of 0.0134°.

4. XMCD experimental results

For the final characterization and commissioning of the setup we selected the $GdCo_2$ compound (Gignoux *et al.*, 1975), which is ferrimagnetic with ordering temperature around 400 K, as a reference sample for XMCD measurements for both a rare-earth L-edge (Gd L_3-edge) and a transition metal K-edge (Co K-edge). Experiments were performed at ambient temperature and ± 1 T applied magnetic field in transmission geometry at both D06A-DXAS dispersive and W09A-XDS non-dispersive beamlines, obtaining equivalent results.

A summary of the XMCD measurements on the $GdCo_2$ sample, using the methods and instrumentation described above, is shown in Fig. 5, obtained at the W09A-XDS beamline. We measured dichroic signals on the same $GdCo_2$ sample, at both the Gd L_3- and Co K-edges, with and without lock-in detection, as compared in Fig. 5. Measurements without lock-in were performed in the static mode: for each energy point, an XAS signal $\ln(I_0/I_1)$ is obtained for the two different beam polarization, and the XMCD is obtained for the signal difference between these two signals. The advantage in signal-to-noise ratio by using the lock-in noise-filtering method is evident from the results, even with the limited photon flux of about 10^{11} photons s^{-1} of these beamlines imposing a limitation on the efficiency of this method. While it is difficult to see a sizable difference in signal-to-noise ratio at the Gd L_3-edge, this becomes clear at the Co K-edge. For low-amplitude XMCD signal, as is the case for the $\sim$15 times less intense signal at the Co K-edge with no spin–orbit coupling at the core level ($l = 0$), the signal-to-noise ratio was evidently improved with the lock-in noise-filtering.

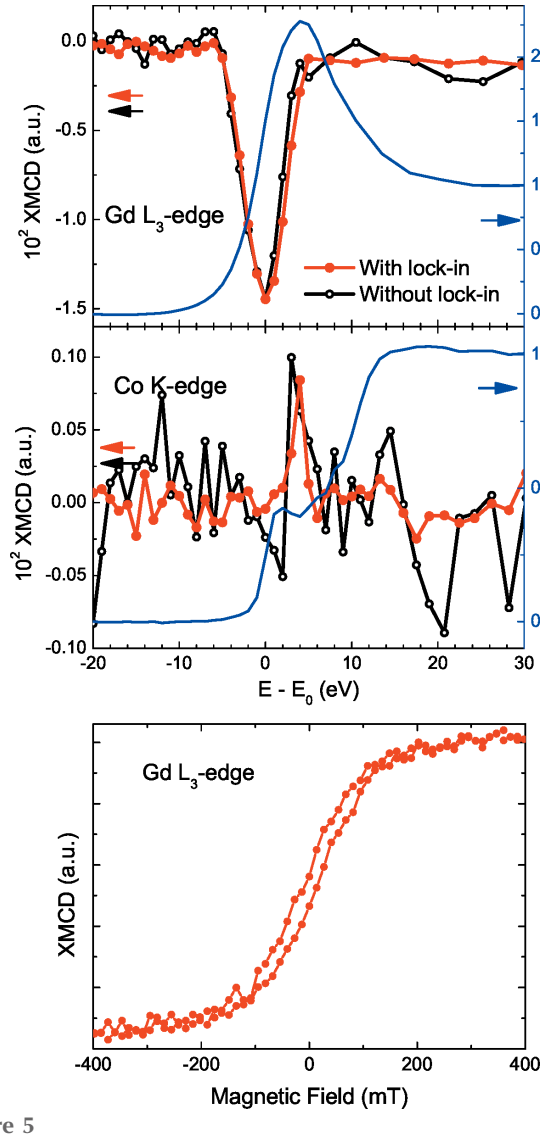

Figure 5
Top: XANES and XMCD signals for $GdCo_2$ at the Gd L_3-edge and Co K-edge. Measurement time for each data set was 40 min. Lock-in frequency was 13 Hz, and the time constant in the lock-in amplifier 100 ms. Bottom: XMCD amplitude as a function of magnetic field for $GdCo_2$, with fixed energy at the XMCD peak of the Gd L_3-edge.

With the ability to perform the XMCD experiment by changing the polarization with the QWP, we were also able to measure the element-selective field dependence of the Gd L_3-edge XMCD amplitude, as shown in Fig. 5, which oftentimes pinpoints crucial magnetic behaviors of the sample depending on the material property of interest. This measurement was obtained for a fixed energy, at the XMCD peak, as a function of the applied magnetic field.

5. Concluding remarks

These results demonstrate that the developed instrumentation successfully allows XMCD measurements to be performed at both dispersive and non-dispersive beamlines with the advantage of using the lock-in noise-filtering. These measurements also show that the implemented geometrical correction, described in Section 3 above, allows a wide energy range only limited by the dispersive polychromator energy bandwidth. For both types of beamline geometries (dispersive-based or intrinsic monochromatic) it is now possible to use large experimental setups such as high-field superconducting magnets using the presented method. This also facilitates XMCD experiments to be performed under high-pressure conditions (Torchio *et al.*, 2014; Haskel *et al.*, 2008; Ishimatsu *et al.*, 2003), since the attenuation by the diamond anvils in this case makes it essential to use the lock-in noise-filtering even for large signals observed under ambient pressure conditions. From our measurements we can estimate an improvement of at least a factor of two on signal-to-noise ratio for experiments with the same measurement time using lock-in detection. Here it is important to note that this improvement was limited for the inherent limitation of a UVX source, second-generation facility, such as soil vibration and low photon flux. Therefore, we believe that this instrumentation will have significantly better results once it is installed at SIRIUS.

The instrumentation was successfully commissioned and made available for external users of XDS or DXAS beamlines. Moreover, this experimental setup is prepared for the undulator-based EMA beamline of the new Brazilian synchrotron source SIRIUS, where more optimized X-ray beam characteristics (*e.g.* beam sizes as small as 100 nm, divergence as small as 20 µrad, photon flux as high as 10^{13} photons s^{-1})

combined with this instrumentation will allow XMCD experiments to be performed at very extreme conditions of applied pressure (Mathon *et al.*, 2004; Haskel *et al.*, 2008; Souza-Neto *et al.*, 2009; Baudelet *et al.*, 2009, 2010; Ishimatsu *et al.*, 2003, 2011; Ishimatsu *et al.*, 2016) as well as low temperatures (<1 K) and high magnetic fields (>10 T) (Uemoto *et al.*, 2001; Strohm *et al.*, 2019). This will allow a plethora of opportunities to study magnetic materials based not only on rare-earth and 3*d* transition metals but also on 4*f* metals (Souza-Neto *et al.*, 2009), 5*d* metals (Laguna-Marco *et al.*, 2010; Veiga *et al.*, 2015), as well as on actinide-based materials (Okane *et al.*, 2008; dos Reis *et al.*, 2017).

Acknowledgements

We are grateful to all LNLS technical and scientific teams that indirectly contributed to this project. Work at LNLS is supported by the Brazilian Ministry of Science and Technology (MCTIC).

Funding information

Funding for this research was provided by: Fundação de Amparo à Pesquisa do Estado de São Paulo (grant No. 2013/22436-5 to Narcizo M. Souza-Neto; grant No. 2014/05480-3 to Narcizo M. Souza-Neto; studentship No. 2014/26620-8 to Eduardo H. T. Poldi; grant No. 2014/26450-5 to Carlos A. Escanhoela Jr.); Conselho Nacional de Desenvolvimento Científico e Tecnológico (studentship No. 136119/2018-2 to Eduardo H. T. Poldi); US Department of Energy, Office of Science (contract No. DE-AC-02-06CH11357).

References

Baudelet, F., Mathon, O., Itié, J.-P., Polian, A., Kappler, J. P. & Pascarelli, S. (2009). *J. Phys. Condens. Matter*, **21**, 346003.
Baudelet, F., Pascarelli, S., Mathon, O., Itié, J.-P., Polian, A. & Chervin, J.-C. (2010). *Phys. Rev. B*, **82**, 140412.
Belyakov, V. & Dmitrienko, V. (1989). *Sov. Phys. Usp.* **32**, 697–719.
Boada, R., Laguna-Marco, M. Á., Gallastegui, J. A., Castro, G. R. & Chaboy, J. (2010). *J. Synchrotron Rad.* **17**, 308–313.
Cezar, J. C., Souza-Neto, N. M., Piamonteze, C., Tamura, E., Garcia, F., Carvalho, E. J., Neueschwander, R. T., Ramos, A. Y., Tolentino, H. C. N., Caneiro, A., Massa, N. E., Martinez-Lope, M. J., Alonso, J. A. & Itié, J.-P. (2010). *J. Synchrotron Rad.* **17**, 93–102.
Chen, C., Idzerda, Y., Lin, H., Smith, N., Meigs, G., Chaban, E., Ho, G., Pellegrin, E. & Sette, F. (1995). *Phys. Rev. Lett.* **75**, 152–155.
Gignoux, D., Givord, F. & Lemaire, R. (1975). *Phys. Rev. B*, **12**, 3878–3884.
Giles, C., Malgrange, C., Goulon, J., de Bergevin, F., Vettier, C., Dartyge, E., Fontaine, A., Giorgetti, C. & Pizzini, S. (1994). *J. Appl. Cryst.* **27**, 232–240.
Haskel, D., Tseng, Y., Souza-Neto, N. M., Lang, J. C., Sinogeikin, S., Mudryk, Ya., Gschneidner, K. A. Jr & Pecharsky, V. K. (2008). *High Pressure Res.* **28**, 185–192.
Hirano, K., Ishikawa, T. & Kikuta, S. (1993). *Nucl. Instrum. Methods Phys. Res. A*, **336**, 343–353.
Hirano, K., Ishikawa, T., Koreeda, S., Fuchigami, K., Kanzaki, K. & Kikuta, S. (1992). *Jpn. J. Appl. Phys.* **31**, L1209–L1211.
Hirano, K., Izumi, K., Ishikawa, T., Annaka, S. & Kikuta, S. (1991). *Jpn. J. Appl. Phys.* **30**, L407–L410.
Ishimatsu, N., Kawamura, N., Maruyama, H., Mizumaki, M., Matsuoka, T., Yumoto, H., Ohashi, H. & Suzuki, M. (2011). *Phys. Rev. B*, **83**, 180409.
Ishimatsu, N., Kawamura, N., Mizumaki, M., Maruyama, H., Sumiya, H. & Irifune, T. (2016). *High. Press. Res.* **36**, 381–390.
Ishimatsu, N., Maruyama, H., Kawamura, N., Suzuki, M., Ohishi, Y., Ito, M., Nasu, S., Kawakami, T. & Shimomura, O. (2003). *J. Phys. Soc. Jpn*, **72**, 2372–2376.
Laguna-Marco, M. A., Haskel, D., Souza-Neto, N. M., Lang, J. C., Krishnamurthy, V. V., Chikara, S., Cao, G. & van Veenendaal, M. (2010). *Phys. Rev. Lett.* **105**, 216407.
Lamirand, A. D., Soares, M. M., Ramos, A. Y., Tolentino, H. C. N., De Santis, M., Cezar, J. C., de Siervo, A. & Jamet, M. (2013). *Phys. Rev. B*, **88**, 140401.
Lang, J. C. & Srajer, G. (1995). *Rev. Sci. Instrum.* **66**, 1540–1542.
Lima, F. A., Saleta, M. E., Pagliuca, R. J. S., Eleotério, M. A., Reis, R. D., Fonseca Júnior, J., Meyer, B., Bittar, E. M., Souza-Neto, N. M. & Granado, E. (2016). *J. Synchrotron Rad.* **23**, 1538–1549.
Mathon, O., Baudelet, F., Itié, J.-P., Pasternak, S., Polian, A. & Pascarelli, S. (2004). *J. Synchrotron Rad.* **11**, 423–427.
Odin, S., Baudelet, F., Itié, J.-P., Polian, A., Pizzini, S., Fontaine, A., Giorgetti, C., Dartyge, E. & Kappler, J. P. (1998). *J. Appl. Phys.* **83**, 7291–7293.
Okane, T., Takeda, Y., Okamoto, J., Mamiya, K., Ohkochi, T., Fujimori, S., Saitoh, Y., Yamagami, H., Fujimori, A., Ochiai, A. & Tanaka, A. (2008). *J. Phys. Soc. Jpn*, **77**, 024706.
Pascarelli, S., Neisius, T. & De Panfilis, S. (1999). *J. Synchrotron Rad.* **6**, 1044–1050.
Reis, R. D. dos, Veiga, L. S. I., Escanhoela, C. A., Lang, J. C., Joly, Y., Gandra, F. G., Haskel, D. & Souza-Neto, N. M. (2017). *Nat. Commun.* **8**, 1203.
Schütz, G., Wagner, W., Wilhelm, W., Kienle, P., Zeller, R., Frahm, R. & Materlik, G. (1987). *Phys. Rev. Lett.* **58**, 737–740.
Souza-Neto, N. M., Haskel, D., Tseng, Y. & Lapertot, G. (2009). *Phys. Rev. Lett.* **102**, 057206.
Stöhr, J. (1999). *J. Magn. Magn. Mater.* **200**, 470–497.
Strohm, C., van der Linden, P., Mathon, O. & Pascarelli, S. (2019). *Phys. Rev. Lett.* **122**, 127204.
Suzuki, M., Inubushi, Y., Yabashi, M. & Ishikawa, T. (2014). *J. Synchrotron Rad.* **21**, 466–472.
Suzuki, M., Kawamura, N., Mizumaki, M., Urata, A., Maruyama, H., Goto, S. & Ishikawa, T. (1998). *Jpn. J. Appl. Phys.* **37**, L1488–L1490.
Suzuki, M., Kawamura, N., Mizumaki, M., Urata, A., Maruyama, H., Goto, S. & Ishikawa, T. (1999). *J. Synchrotron Rad.* **6**, 190–192.
Tolentino, H. C. N., Cezar, J. C., Souza-Neto, N. M. & Ramos, A. Y. (2005). *J. Synchrotron Rad.* **12**, 168–176.
Torchio, R., Mathon, O. & Pascarelli, S. (2014). *Coord. Chem. Rev.* **277–278**, 80–94.
Uemoto, S., Maruyama, H., Kawamura, N., Uemura, S., Kitamoto, N., Nakao, H., Hara, S., Suzuki, M., Fruchart, D. & Yamazaki, H. (2001). *J. Synchrotron Rad.* **8**, 449–451.
Veiga, L. S. I., Fabbris, G., van Veenendaal, M., Souza-Neto, N. M., Feng, H. L., Yamaura, K. & Haskel, D. (2015). *Phys. Rev. B*, **91**, 235135.